

Swarm UAV SAR for 3-D Imaging: System Analysis and Sensing Matrix Design

Hang Ren^{ID}, *Graduate Student Member, IEEE*, Zhichao Sun^{ID}, *Member, IEEE*, Jianyu Yang^{ID}, *Member, IEEE*,
Yuping Xiao, *Student Member, IEEE*, Hongyang An, *Graduate Student Member, IEEE*,
Zhongyu Li^{ID}, *Member, IEEE*, and Junjie Wu^{ID}, *Member, IEEE*

Abstract—The unmanned aerial vehicle (UAV) is a low-cost and high-efficiency lightweight synthetic aperture radar (SAR)-mounted platform that can be used for a variety of military and civilian missions. Using multiple UAVs to form a swarm can break through the limitations of a single platform and has broad application prospects. In this article, swarm UAV SAR that contains tens or hundreds of UAV platforms is proposed for the first time. The concept and advantages of swarm UAV SAR are investigated, and the mission outlook is given. Afterward, the swarm UAV 3-D linear array SAR (LASAR) is illustrated, which enables high-resolution 3-D imaging in a single flight. Since the antenna array of the swarm UAV 3-D LASAR is sparse, the compressed sensing (CS) algorithm is applied, whose reconstruction performance is closely related to the correlation coefficient of the sensing matrix. Hence, the signal model of swarm UAV 3-D LASAR is derived, and the expression of the sensing matrix is deduced. The sensing matrix design in this article aims at obtaining satisfactory reconstruction performance by optimizing the distribution of the antenna elements, which directly influences the correlation coefficient of the sensing matrix. Considering the limitation of the practical conditions, the sensing matrix design problem is modeled as a constrained integer programming problem. Finally, a sensing matrix design method based on discrete constrained differential evolution (DCDE) algorithm is proposed to solve the optimization problem. Experimental results demonstrate the effectiveness and superiority of the proposed method.

Index Terms—3-D imaging, compressed sensing (CS), differential evolution, sensing matrix design, Swarm unmanned aerial vehicle (UAV) synthetic aperture radar (SAR).

I. INTRODUCTION

SYNTHETIC aperture radar (SAR) has been greatly developed and widely applied in military and civilian applications due to its all-day, all-weather, and high-resolution observation capability [1], [2]. The unmanned aerial vehicle (UAV) SAR is able to accomplish various kinds of advanced missions, such as urban monitoring, agricultural

Manuscript received 16 May 2022; revised 2 September 2022 and 18 October 2022; accepted 8 November 2022. Date of publication 14 November 2022; date of current version 23 November 2022. This work was supported in part by the National Natural Science Foundation of China under Grant 61901088, Grant 61922023, Grant 61771113, and Grant 62171084; and in part by the China Postdoctoral Science Foundation under Grant 2020M683292, Grant 2019M65338, and Grant 2019TQ0052. (Corresponding authors: Zhichao Sun; Jianyu Yang.)

The authors are with the School of Information and Communication Engineering, University of Electronic Science and Technology of China, Chengdu 611731, China (e-mail: threadkite@sina.com; jyyang@uestc.edu.cn).

Digital Object Identifier 10.1109/TGRS.2022.3221775

plant protection, and buried target detection [3]. Compared to large platforms used in traditional SAR systems, such as aircrafts and satellites, the UAV platform has the advantages of low cost, flexible deployment, and easy operation [4]. Current studies on UAV SAR includes motion error compensation [5], [6], [7], imaging methods [8], [9], [10], path planning [11], [12], and so on.

Due to the outstanding advantages, UAV is an ideal platform for multistatic/swarm SAR, which is capable of diverse missions including 3-D imaging. Compared with monostatic/bistatic SAR, swarm UAV SAR has some new benefits. First, the swarm UAV SAR system has superior coordination, intelligence, and autonomy [6]. It is highly flexible and reconfigurable due to the use of decentralized communication networks. Second, utilizing swarm intelligence-based damage-resilient mechanism, swarm UAV SAR is able to complete dangerous missions with high cost effectiveness and robustness [13]. Last but not least, swarm UAV SAR can be divided into multiple subswarms for simultaneous multitasking [14]. With the increasing application demands, numerous studies on multistatic SAR have been conducted, which mainly focus on system analysis [15], [16], configuration design [17], [18], synchronization method [19] and imaging algorithm [20], [21]. Besides, some studies have been devoted to new multistatic applications. For instance, the multistatic multispect SAR data acquisition is stated to improve the radar image interpretation in [22]. A frequency-domain registration method is proposed for multistatic multifrequency SAR in [23]. However, the potential of swarm UAV SAR is still not fully explored, and few studies have mentioned the advanced multistatic 3-D SAR imaging working mode to the best of our knowledge.

3-D SAR imaging has great application potential in urban mapping [24], pipeline detection and localization [25], target recognition [26], and so on. Generally, traditional 3-D SAR can be categorized into three types: curvilinear SAR (CSAR), tomography SAR (TomoSAR), and linear array SAR (LASAR). Thereinto, CSAR is often difficult to achieve the ideal curve trajectory to obtain the ideal 3-D resolution [27], [28], [29], [30], and TomoSAR loses real-time processing capability due to multiple flight times [31], [32], [33]. LASAR controls the linear array antenna movement in space to form a virtual 2-D array and combines the pulse compression technology to obtain the 3-D resolution of the observation

target [34], [35]. It is not limited by the trajectory of the moving platform and the number of navigations, and has the characteristics of flexible imaging, compared with CSAR and TomoSAR [36]. However, the cross-track resolution of traditional LASAR is limited by the wingspan.

Swarm UAV 3-D LASAR utilizes multiple platforms, each carrying multiple antenna elements, to form a large sparse linear antenna array to obtain 3-D information. It breaks through the limitation of array length to obtain high resolution compared to LASAR. Due to the sparse antenna array, compressed sensing (CS) theory should be applied to multistatic 3-D imaging [37], [38]. The CS recovery performance is closely related to the correlation coefficient of the sensing matrix [39], [40], [41]. By adjusting the multiplatform antenna arrangement in a swarm UAV 3-D LASAR system, the correlation coefficient of the sensing matrix is changed. Therefore, the problem arises as to how to design an optimal antenna arrangement in order to obtain the desired sparse reconstruction performance, which is the purpose of the swarm UAV 3-D LASAR mission design. In this article, the swarm UAV SAR system is first put forward. The system concept of swarm UAV SAR is explained, and its motivation and advantages are analyzed in detail. Various missions, which can be executed by swarm UAV SAR system, including 3-D imaging, simultaneous multispect observation, and multifrequency observation, are illustrated. Afterward, the swarm UAV 3-D LASAR system for 3-D imaging is introduced. Since the traditional monostatic model cannot be used in the multistatic configurations, the multistatic range model and signal model of swarm UAV 3-D LASAR is derived. Then, the expression of the sensing matrix is given, and the correlation coefficient of the sensing matrix is derived accordingly. Finally, the mission design problem of the swarm UAV 3-D LASAR is modeled as a constrained optimization problem, and a sensing matrix design method based on discrete constrained differential evolution (DCDE) algorithm is proposed to solve the problem.

The rest of this article is organized as follows. In Section II, the swarm UAV SAR system concept is elaborated, the system advantages are analyzed, and three missions are illustrated. In Section III, the signal model of swarm UAV 3-D LASAR is established, and the correlation coefficient of the sensing matrix is deduced. In Section IV, the sensing matrix design problem is modeled, and a mission design method based on CDE) algorithm is proposed for solving it. In Section V, simulation results are given. Section VI concludes this article.

II. SWARM UAV SAR SYSTEM

A. System Concept

Swarm UAV SAR system, as illustrated in Fig. 1, contains tens or hundreds of spatially separate transmitting and receiving UAV platforms. Each UAV platform is loaded with an SAR payload, a positioning module, a synchronization module, a communication module, and a flying control system. UAVs collaborate with each other to accomplish complex imaging tasks. The system relies on communication links to achieve interconnection and form the swarm UAV network, where each UAV platform is abstracted as a node. The attributes of the

nodes are stored in the routing table, through which each node in the entire network obtains information about its neighbors. By refreshing the routing table, the entire network structure can be updated so that the system has dynamic reconfiguration capability. Moreover, the swarm UAV system adopts a decentralized network, where each node has sufficient information transmission capabilities to become the information fusion and control center of the entire network. Through the decentralized communication network, the ground station is able to implement collaborative multitask planning and quickly adjust the mission allocation based on the actual requirements and real-time situation. According to the mission planning, the UAV swarm can be divided into multiple subswarms to complete different tasks simultaneously.

A typical working scenario of the swarm UAV SAR system is illustrated in Fig. 1, where the observation mission requires multispect observation and 3-D imaging simultaneously. First, decision-making involving evaluation and assignment of tasks is conducted. Afterward, the ground station generates corresponding subtask planning paths based on the decision data. Instructions are loaded on the UAV platforms, and then, the swarms begin to execute the tasks. In swarm1, one UAV transmits the signal and the other UAVs receive the signal from different directions to complete simultaneous multispect observation. The preprocessed echo data, synchronization information, and motion parameters are transmitted to the ground station for signal processing, imaging, and interpreting. In case some UAVs are damaged during the mission, redundant UAVs are always ready for reconfiguring. Furthermore, the damage-resilient method is utilized to reorganize the UAVs and ensure that the swarm functions properly. In swarm2, the fixed-wing UAVs fly in formation to form a large sparse 2-D antenna array. Swarm2 cooperates with an external spaceborne transmitter to complete 3-D imaging in complex terrain. Moreover, UAVs in swarm2 cooperate with each other through the communication network. First, the multirotor UAVs mounted with optical cameras and laser radars are utilized for detection. If these UAVs find out that the terrain of the target scene becomes complicated, the fixed-wing UAVs begin to receive the echo signal for 3-D imaging. The processed 3-D information, in turn, helps the UAVs in swarm2 to adjust their flight paths to avoid collisions.

B. Motivations and Advantages

In recent years, the miniaturization of SAR hardware system chips offers a great opportunity to mount SAR systems on UAV platforms. UAVs can be formed into networks to realize a variety of different advanced SAR missions, which offers the potential of exceeding the capabilities of monostatic/bistatic SAR systems in various ways. The advantages of the swarm UAV SAR system are given as follows.

- 1) By transmitting different frequency signals at different angles, swarm UAV SAR is able to access more comprehensive scattering information, which enables the system to repress the noise and obtain better resolution [42]. Compared with scattering information obtained from a single angle, the comprehensive scattering characteristic

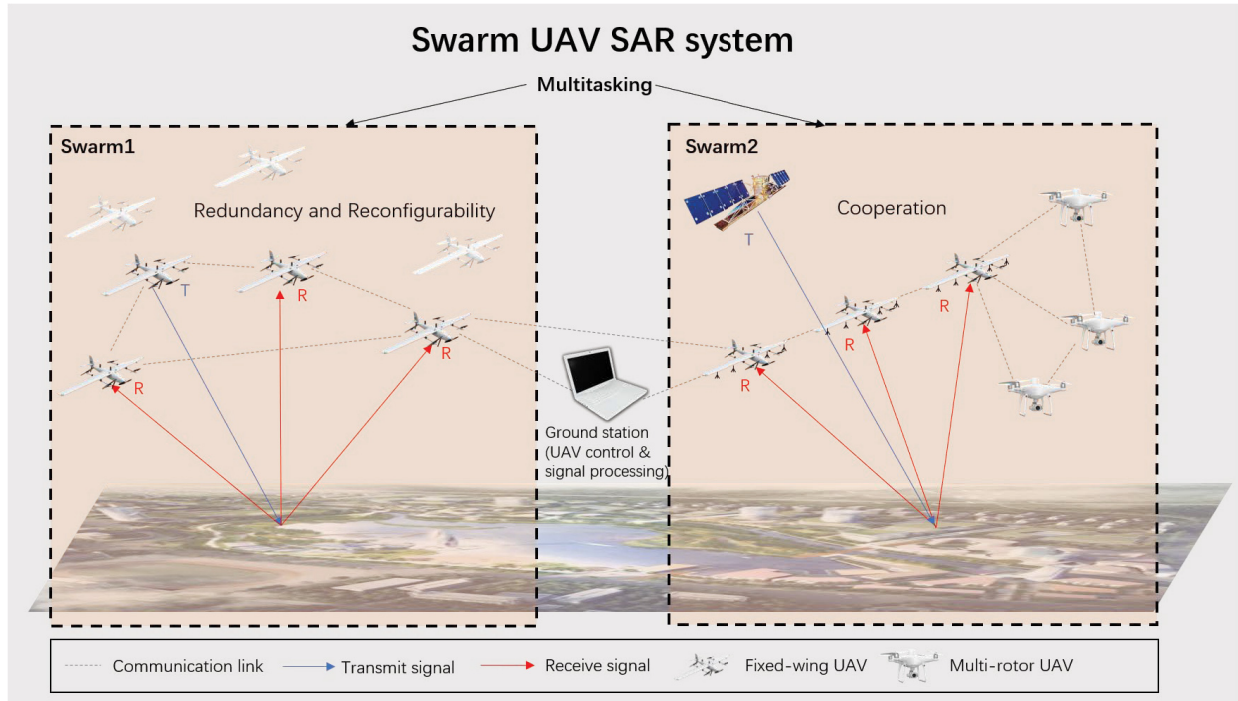


Fig. 1. Illustration of the swarm UAV SAR system concept.

information of targets provides better image interpretation, terrain classification, and target identification capability [43], [44].

- 2) Swarm UAV SAR is centerless, morphologically, and functionally reconfigurable, which indicates that it has strong resistance to damage.
- 3) Due to the high degree of flexibility and diversity of the time-varying configuration, swarm UAV SAR is able to achieve diverse complicated civilian or military missions simultaneously compared with monostatic/bistatic SAR.
- 4) The swarm UAV SAR system is cost-effective compared with multistatic airborne/spaceborne SAR. It also has the advantages of small size, lightweight, and brisk movement, which makes it easily accessible and rapidly deployable.
- 5) Swarm UAV SAR may cooperate with other traditional transmit platforms to expand application scope and scenarios. For instance, geosynchronous SAR (GEO-SAR) can be utilized as a stable, reliable, and safe illuminator for swarm UAV SAR [45].

C. Challenges

Though the swarm UAV SAR system has unparalleled advantages, it also faces challenges in many aspects, including communication, collaboration, formation, and so on. The following will elaborate on the challenges faced by the swarm UAV SAR system.

- 1) In the swarm UAV SAR system, a considerable amount of data needs to be transmitted for SAR imaging. Besides, multiple UAVs need to exchange information in order to improve the efficiency of coordinated task completion. Therefore, it is one of the major challenges

to design a communication network, which can meet the needs of timely and complete information transmission, and allocate communication resources under certain communication topology [46].

- 2) Separation of transceiver platforms in swarm UAV SAR systems brings problems of space, time, and phase synchronization. The illumination method and precision of the transmit and receive beams will affect the spatial synchronization performance, resulting in a decrease in coherence. If the receiving end and the transmitting end use independent reference frequencies, their differences will introduce time synchronization errors and phase synchronization errors, resulting in the degradation of imaging performance [47]. Therefore, it is necessary to focus on the synchronization methods, including the direct wave synchronization method, the method of transmitting a synchronization signal by establishing a communication or synchronization chain, and so on.
- 3) Both the SAR imaging performance and the communication performance of the swarm UAV SAR system are closely related to the configuration of the swarm UAV. Mathematically, maintaining the optimal configuration of a UAV swarm can be regarded as a challenging time-varying formation problem for high-order swarm systems [48].

D. Mission Overview

Swarm UAV SAR can accomplish a variety of different missions, including simultaneous multispectra observation, multifrequency observation, 3-D imaging, and so on, which will be introduced in the following.

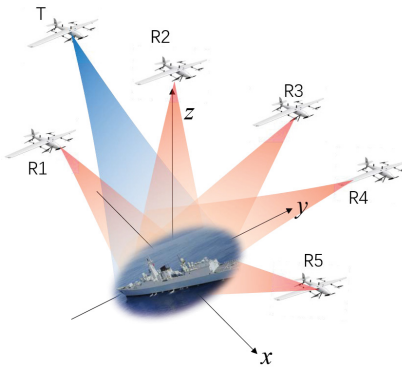


Fig. 2. Schematic of the simultaneous multiaspect observation.

1) Simultaneous Multiaspect Observation: Multiaspect observation [49] means imaging of the same target or scene from a different azimuth and elevation. As depicted in Fig. 2, swarm UAV SAR can achieve simultaneous multiaspect observation by distributing multiple UAV receivers in different locations. Compared with traditional SAR, multiaspect SAR has the advantage of spatial diversity. Expanding the space spectrum support area of the detected target can avoid the problems of target shading and layover distortion in traditional SAR and improve the classification and recognition ability of targets. Multiaspect SAR measurement can be divided into two major categories. One is multiaspect SAR observation based on a single platform. In this case, the system detects fixed targets from different angles at different times. It has a simple system structure but can only work under the condition that the electromagnetic scattering properties of the imaging region do not change fundamentally. In other words, it has limited adaptability to rapidly changing target scenarios. The other is simultaneous multiaspect SAR observation. It utilizes a distributed SAR system to detect the target scene simultaneously. It has a relatively complicated system structure but is applicable to a wider range of imaging scene types. The rapid development of UAVs provides convenience for simultaneous multiaspect SAR observation, which has low requirements for scene stability. UAV is small in size, easy to control, and can safely approach the target scene to obtain multiaspect SAR data in a short time. Thus, it is highly cost-effective to apply a swarm UAV SAR system for simultaneous multiaspect observation.

2) Multifrequency Observation: The schematic of the multifrequency observation is depicted in Fig. 3, where each UAV transmits and receives signals in different frequency bands. The radar scattering characteristic of targets is closely related to the operation frequency [50]. Specifically, when the SAR operating frequency is high, the SAR image texture features are obvious, and it is easy to obtain the surface fine structure information of ground objects. When the SAR operating frequency band is low, the SAR system has better penetration capability to discover the concealed targets [51]. The multifrequency SAR system can synthesize the information from SAR images of different frequency bands and fuse a false color image for image interpretation and target

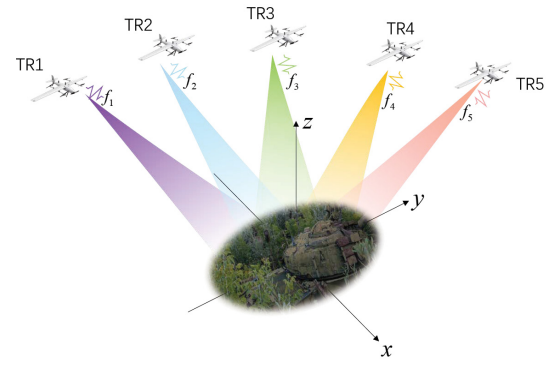


Fig. 3. Schematic of the multifrequency observation.

recognition. Compared to monostatic SAR, swarm UAV SAR can achieve multifrequency observation with a simple system design, as transmitting antennas of different frequencies are mounted on different platforms. Furthermore, swarm UAV SAR can easily fulfill the multifrequency observation and the multiaspect observation simultaneously.

3) 3-D Imaging: 3-D imaging technique utilizes 3-D information of the observed target to fully reflect the 3-D structure of the target. In this article, LASAR [34] is combined with the swarm UAV SAR system, which is called swarm UAV 3-D LASAR, where multiple UAV platforms are deployed to form a large sparse linear array. Traditional monostatic LASAR faces the defect of poor cross-track resolution due to the limitation of the wingspan. In swarm UAV 3-D LASAR, the length of the linear antenna array breaks through the limitation of platform space by combining the array elements carried by UAVs into a large sparse array. As the antenna array's length increases, the cross-track resolution of the swarm UAV LASAR improves significantly compared with monostatic LASAR. In addition, swarm UAV 3-D LASAR can be conveniently combined with various kinds of transmitting platforms according to the actual demand and can work in the forward-looking mode. Therefore, it has a broader application prospect. Section III will introduce the swarm UAV 3-D LASAR in detail.

III. SWARM UAV 3-D LASAR SYSTEM

A. Signal Model and Range History

The schematic of the imaging geometry of swarm UAV 3-D LASAR is shown in Fig. 4. Multiple UAV platforms, each carrying one or multiple receiving antennas to form a large sparse linear array, are supposed to fly at the altitude H_R along the flight path. The transmitting antenna can be mounted on UAV/aircraft/satellite. Axes X, Y, and Z are the along-track, cross-track, and height directions, respectively, which are orthogonal to each other. The swarm UAV 3-D LASAR system can work in the forward-/downward-looking mode.

The geometric model of the 2-D sparse antenna array is illustrated in Fig. 5. The colored dots represent the element position corresponding to a full uniform linear array. The blue dot means that an actual antenna element exists in the element position, while the red dot denotes that the corresponding

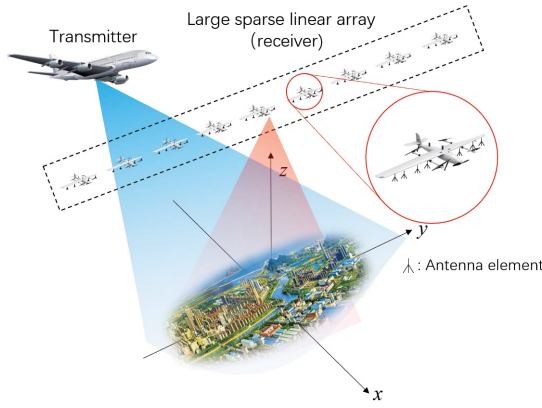


Fig. 4. Schematic of the imaging geometric model of swarm UAV 3-D LASAR.

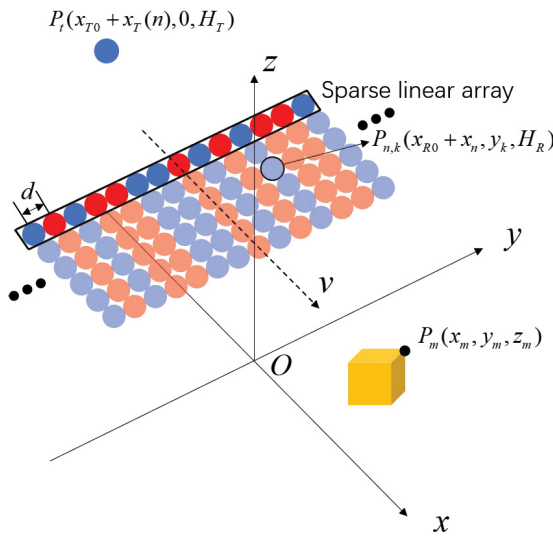


Fig. 5. Geometric model of 2-D sparse antenna array. The blue dot means that there exists an antenna element; the red dot means that the antenna element is vacant.

element position is vacant. It is necessary to point out that some positions should be vacant because of the minimum flight spacing constraint, while other positions can either be vacant or occupied. The sparse linear array moves along the x -axis to form a 2-D virtual sparse array for 3-D imaging. Assume that a point target is located at $P_m = (x_m, y_m, z_m)$ with scattering coefficient $\alpha(P_m)$. The k th receiving antenna at the n th slow time is located at $P_{n,k} = (x_{R0} + x_n, y_k, H_R)$, where H_R is the antenna height.

If the target is situated at the far-field of the receiving antenna, the slant range R_R can be approximated as

$$\begin{aligned} R_R(n, k; P_m) &= R_{R0} \sqrt{1 + \frac{u_R(n, k, m)}{R_{R0}^2}} \\ &\approx R_{R0} \left(1 + \frac{u_R(n, k, m)}{2R_{R0}^2} - \frac{1}{8} \left(\frac{u_R(n, k, m)}{R_{R0}^2} \right)^2 \right) \end{aligned} \quad (1)$$

where $R_{R0} = (H_R^2 + x_{R0}^2)^{1/2}$ is the range from the antenna array center to the scene center, and $u_R(n, k, m) = (x_n - x_m)^2 + 2x_{R0}(x_n - x_m) + (y_k - y_m)^2 + z_m^2 - 2H_R z_m$.

Similarly, the slant range from P_m to the transmitting antenna $P_T = (x_{T0} + x_T(n), 0, H_T)$ at the n th slow time can be formulated as

$$R_T(n; P_m) \approx R_{T0} \left(1 + \frac{u_T(n, m)}{2R_{T0}^2} - \frac{1}{8} \left(\frac{u_T(n, m)}{R_{T0}^2} \right)^2 \right) \quad (2)$$

where $R_{T0} = (H_T^2 + x_{T0}^2)^{1/2}$ is the range from the transmitter to the center of the scene, and $u_T(n, m) = (x_T(n) - x_m)^2 + 2x_{T0}(x_T(n) - x_m) + y_m^2 + z_m^2 - 2H_T z_m$.

The total time delay from the target point P_m to the k th receiving antenna and the transmitting antenna at the n th slow time can accordingly be formulated as

$$\tau(n, k; P_m) = \frac{R_R(n, k; P_m) + R_T(n; P_m)}{c} \quad (3)$$

where c is the speed of light.

According to the electromagnetic scattering approximation [52], the echo signal $S(l, n, k)$ at high frequency can be approximated as the superposition of the echo responses of all independent scattering centers in the imaging space. Thus, the total echo signal of the k th antenna at the n th slow time can be expressed as

$$\begin{aligned} S(l, n, k) &= \sum_{m=1}^{M_E} S(l, n, k; P_m) \\ &= \sum_{m=1}^{M_E} \{ \alpha(P_m) \exp(-j2\pi f_c \tau(n, k; P_m)) \\ &\quad \times \exp(j\pi K_r [t(l) - \tau(n, k; P_m)]^2) \} \\ &= \overrightarrow{\psi_s(l, n, k)}^T \cdot \overrightarrow{\alpha_s} \end{aligned} \quad (4)$$

where l is the fast time serial number, n is the slow time serial number, K_r is the frequency modulation rate, f_c is the center frequency, M_E is the total number of resolution units divided in the corresponding 3-D scene, and $\alpha(P_m)$ is the scattering coefficient of the m th resolution unit. $\overrightarrow{\alpha_s}$ is the scattering coefficient vector, and $\overrightarrow{\psi_s(l, n, k)}$ represents the corresponding time delay phase measurement vector, which is presented as in (6), shown at the bottom of the next page.

Represent all 3-D echo signal as a vector $\overrightarrow{y_s}$, whose expression can be presented as

$$\overrightarrow{y_s} = \text{Vec}\{S(l, n, k)\}. \quad (5)$$

Therefore, the linear measurement model of the whole scene echo signal can be expressed as $\overrightarrow{y_s} = F_S \cdot \overrightarrow{\alpha_s} + \overrightarrow{n_s}$, where $\overrightarrow{n_s}$ is the noise vector, and the measurement matrix F_S is formulated as in (7), shown at the bottom of the next page.

B. Correlation Coefficient of the Sensing Matrix

In the traditional LASAR system, the antenna elements should be compactly distributed to meet the Nyquist sampling rate for signal recovery. Therefore, it needs plenty of platforms to carry antenna elements, which results in a high cost-efficiency ratio. Besides, massive data in traditional

LASAR greatly increase the cost of storage, transmission, and processing. The CS theory has pointed out that sparse signals can be well reconstructed using only a small number of linear measurements compared with traditional methods. There are a large number of nontarget areas in the 3-D imaging space, such as atmospheric areas and electromagnetic wave shielding areas. Consequently, the target scatterers are sparsely distributed in the 3-D imaging space [53]. Thus, the swarm UAV 3-D LASAR system utilizes CS for 3-D imaging in order to reduce the cost. Given the 3-D echo signal vector \vec{y}_s and the measurement matrix F_s , the 3-D sparse imaging is transformed into a complex domain l_0 -norm minimization problem, which can be formulated as

$$\min \|\vec{\alpha}_s\|_0 \quad \text{s.t.} \quad \|\vec{y}_s - F_s \vec{\alpha}_s\|_2 \leq \varepsilon \quad (8)$$

where ε is the noise level in echo signal \vec{y}_s and F_s is the sensing matrix in the problem. The l_0 -norm minimization problem can be transformed into an iterative problem and then solved by iterative greedy pursuit techniques, such as orthogonal matching pursuit (OMP), or it can be approximated as a l_1 -norm minimization problem and be solved by the convex relaxation techniques, such as basic pursuit (BP).

The restricted isometry property (RIP) is a popular measure to establish the tightest performance guarantees. However, the RIP calculation is an NP-hard problem. As a search must be performed for all combinations, it is very difficult to compute the restricted isometry constants of a sensing matrix in practice, especially when the dimension of the sensing matrix or the sparsity level is large. The correlation coefficient of the sensing matrix F_s is a more practical measure for assessing the CS recovery properties [39]. It is fundamentally related to the restricted isometry constants, while it also has the advantage of low computation. The smaller the correlation coefficient of the sensing matrix is, the higher the probability of accurately reconstructing the target scattering coefficients. The correlation coefficient of the sensing matrix F_s can be presented as

$$\mu(F_s) = \max_{i \neq j} \frac{|\langle \chi_i, \chi_j \rangle|}{\|\chi_i\|_2 \|\chi_j\|_2} \quad (9)$$

where χ_i and χ_j represent the i th and j th columns of the sensing matrix, respectively.

According to the signal model in Section III-A, the correlation expression between χ_i and χ_j can be formulated as

$$\begin{aligned} & \langle \chi_i, \chi_j \rangle \\ &= \sum_{n=1}^{N_A} \sum_{k=1}^{N_C} \sum_{l=1}^{N_R} \exp(-j2\pi f_c(\tau(n, k; P_i) - \tau(n, k; P_j))) \end{aligned}$$

$$\vec{\psi}_s(l, n, k) = \left[\begin{array}{c} \exp(-j2\pi f_c \tau(n, k; P_1)) \cdot \exp(j\pi K_r[t(l) - \tau(n, k; P_1)]^2) \\ \exp(-j2\pi f_c \tau(n, k; P_2)) \cdot \exp(j\pi K_r[t(l) - \tau(n, k; P_2)]^2) \\ \vdots \\ \exp(-j2\pi f_c \tau(n, k; P_{M_E})) \cdot \exp(j\pi K_r[t(l) - \tau(n, k; P_{M_E})]^2) \end{array} \right] \quad (6)$$

$$F_s = \left[\vec{\psi}_s(1, 1, 1), \dots, \vec{\psi}_s(N_R, 1, 1), \dots, \vec{\psi}_s(1, N_A, 1), \dots, \vec{\psi}_s(N_R, N_A, 1), \dots, \vec{\psi}_s(1, N_A, N_C), \dots, \vec{\psi}_s(N_R, N_A, N_C) \right]^T \quad (7)$$

$$\begin{aligned} & \times \exp(j\pi K_r[t(l) - \tau(n, k; P_i)]^2 \\ & - j\pi K_r[t(l) - \tau(n, k; P_j)]^2) \end{aligned} \quad (10)$$

Since the integral of the range delay function is equivalent to the matched filter compression of the range signal, the correlation expression can be formulated as

$$\begin{aligned} & \langle \chi_i, \chi_j \rangle \\ &= N_R \chi_R(\Delta R(P_i, P_j)) \sum_{n=1}^{N_A} \sum_{k=1}^{N_C} \exp(-jK_0(\Delta R(n, k; P_i, P_j))) \\ &= N_R N_A N_C \chi_R(\Delta R(P_i, P_j)) \chi_{A-C}(\Delta R(P_i, P_j)) \end{aligned} \quad (11)$$

where $\chi_R(P_i, P_j)$ and $\chi_{A-C}(P_i, P_j)$ represent the range dimension and the array plane dimension ambiguity function, respectively, N_A represents the number of slow time, N_C represents the number of antennas, N_R represents the number of quick time, $K_0 = 2\pi/\lambda$ represents the wavenumber, $\Delta R(P_i, P_j) = \Delta R_R(n, k; P_i, P_j) + \Delta R_T(n; P_i, P_j)$ represents the total range difference between P_i and P_j , and $\Delta R_R(n, k; P_i, P_j)$ and $\Delta R_T(n; P_i, P_j)$ represent the range difference between P_i and P_j to the k th receiving antenna and that to the transmitting antenna at the n th slow time, respectively, whose expressions can be formulated as

$$\begin{aligned} & \Delta R_R(n, k; P_i, P_j) \\ &= R_R(n, k; P_i) - R_R(n, k; P_j) \\ &\approx \frac{(2x_n + 2x_{R0} - x_i - x_j)(x_j - x_i)}{2R_{R0}} \\ &+ \frac{(2y_k - y_i - y_j)(y_j - y_i)}{2R_{R0}} + \frac{(2H_R - z_i - z_j)(z_j - z_i)}{2R_{R0}} \\ &- \frac{(2x_n - x_i - x_j)(x_j - x_i)}{2R_{R0}} \cdot \frac{x_{R0}^2}{R_{R0}^2} \end{aligned} \quad (12)$$

$$\begin{aligned} & \Delta R_T(n; P_i, P_j) \\ &= R_T(n; P_i) - R_T(n; P_j) \\ &\approx \frac{(2x_T(n) + 2x_{T0} - x_i - x_j)(x_j - x_i)}{2R_{T0}} \\ &+ \frac{(-y_i - y_j)(y_j - y_i)}{2R_{T0}} + \frac{(2H_T - z_i - z_j)(z_j - z_i)}{2R_{T0}} \\ &- \frac{(2x_T(n) - x_i - x_j)(x_j - x_i)}{2R_{T0}} \cdot \frac{x_{T0}^2}{R_{T0}^2}. \end{aligned} \quad (13)$$

Note that (12) and (13) are derived under the assumption that the target is located at the far-field of the radar. Besides, (12) and (13) ignore the quadratic terms and higher order terms of $1/R_{T0}$ and $1/R_{R0}$. In LASAR, the relative position of linear antenna elements usually does not change

with slow time. In other words, there are no coupling terms for k and n in the array plane dimension ambiguity function. Therefore, we have

$$\chi_{A-C}(\Delta R(P_i, P_j)) = \chi_A(\Delta R(P_i, P_j))\chi_C(\Delta R(P_i, P_j)) \quad (14)$$

where $\chi_C(\Delta R(P_i, P_j))$ and $\chi_A(\Delta R(P_i, P_j))$ represent the cross- and along-track ambiguity functions, respectively.

Substitute (12) and (13) into (10); the absolute values of $\chi_C(\Delta R(P_i, P_j))$ and $\chi_A(\Delta R(P_i, P_j))$ can be formulated as

$$|\chi_C(\Delta R(P_i, P_j))| = \frac{1}{N_C} \left| \sum_{k=1}^{N_C} \exp \left(-j K_0 \frac{y_k(y_j - y_i)}{R_{R0}} \right) \right| \quad (15)$$

$$|\chi_A(\Delta R(P_i, P_j))| = \frac{1}{N_A} \left| \sum_{n=1}^{N_A} \exp(-j K_0 a \cdot (x_j - x_i)) \right| \quad (16)$$

where $a = ((x_T(n)H_T^2)/(R_{T0}^3)) + ((x_nH_R^2)/(R_{R0}^3))$. From (15), we can discover that the cross-track ambiguity function is closely related to each antenna element's position y_k . In other words, the sparse reconstruction performance can be significantly improved by designing the optimal antenna arrangement.

IV. SENSING MATRIX DESIGN VIA DISCRETE CONSTRAINED DIFFERENTIAL EVOLUTION

A. Problem Modeling

As mentioned above, the reconstruction performance is closely related to the correlation coefficient of the sensing matrix, which can be formulated as

$$\mu(F_S) = \max_{i \neq j} |\chi_R(\Delta R)\chi_A(\Delta R)\chi_C(\Delta R)| \quad (17)$$

where $\chi_R(\Delta R)$ and $\chi_A(\Delta R)$ are not affected by the position distribution of the antenna elements. Therefore, the correlation coefficient only depends on the absolute value of the cross-track ambiguity function in swarm UAV 3-D SAR, which can be formulated as

$$|\chi_C(\Delta R)| = \frac{1}{N} \left| \sum_{k=1}^{N_C} \beta_k \exp \left(-j K_0 \frac{d(k-1)(y_j - y_i)}{R_{R0}} \right) \right| \quad (18)$$

where d is the spacing between adjacent optional position, β_k is the array's excitation coefficient, and $\beta_k \in \{0, 1\}$. If the k th position is selected for mounting an antenna element, $\beta_k = 1$; otherwise, $\beta_k = 0$. N is the number of actual antenna elements in the system, and N_C is the total number of optional element positions in a uniform linear array.

The aim is to design an optimal sparse antenna array with a low correlation coefficient. Therefore, the mission design problem can be formulated as

$$\begin{aligned} & \arg \min_{\beta_k} \max_{i \neq j} \left| \sum_{k=1}^{N_C} \beta_k \exp \left(-j K_0 \frac{d(k-1)(y_j - y_i)}{R_{R0}} \right) \right| \\ & \text{s.t. } C1 : \sum_{k=1}^{N_C} \beta_k = N \\ & \quad C2 : \beta_k = 0, k \bmod (l+m) = 0 \parallel k \bmod (l+m) > l \end{aligned} \quad (19)$$

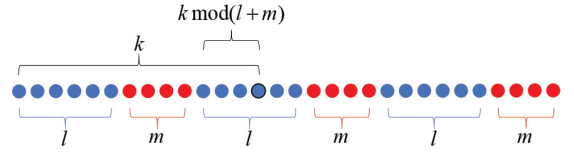


Fig. 6. Illumination about the relation between k , l , and m . The blue dot means that this is an optional position; the red dot means that this is an unavailable position.

where l is the number of optional positions on a UAV platform, m is the number of unavailable positions between adjacent UAVs, and $k \bmod (l+m)$ represents the remainder of $l+m$ for k , as shown in Fig. 6. $C1$ means that totally N positions should be mounted with antenna elements. $C2$ is the spacing constraint requiring that the positions located between the adjacent platforms cannot be mounted with an antenna element.

B. Sensing Matrix Design Method Based on DCDE

The optimization problem (19) is a constrained single-objective optimization problem (CSOP) [54], where β_k is the decision variable whose value is either 1 or 0, indicating that the optimization problem is also an integer programming problem [55]. Traditional methods, including the branch and bound method, the cut plane method, and the implicit enumeration method, have been proposed for solving low-dimensional integer programming problems [56], [57], [58]. However, for large-scale problems, those traditional methods are time-consuming since the computational cost grows exponentially as the number of variables increases. Besides, these methods have difficulty in handling the constraints. The constrained differential evolution (CDE) algorithm is an efficient state-of-the-art method to solve CSOPs [59]. However, CDE algorithms are designed for solving CSOP with continuous decision space, which means that those algorithms cannot be utilized directly for solving discrete integer programming problems. Therefore, a sensing matrix design method based on the DCDE algorithm is proposed in this section. The framework of the sensing matrix design method is presented in Algorithm 1, and its main procedures are presented as follows.

First, the system parameters should be specified according to the actual conditions. The system parameters include the wavelength λ , the spacing between adjacent optional position d , the range from the antenna array center to the scene center R_{R0} , the total number of positions N_C , the number of actual antenna elements N , the number of optional positions on a UAV l , and the number of unavailable positions between adjacent UAVs m . After problem specification, the algorithm parameters are set, and the initial population P_0 is randomly generated.

The novelty of DCDE is that it proposes the discretization (trait expression) procedure. Once an individual is generated, it should be interpreted by discretization. An individual consists of N_C continuous real variables. Each continuous real variable x_j can be transformed to its corresponding discrete

Algorithm 1 Sensing Matrix Design Method Based on DCDE

- 1: Specify the system parameters according to the actual conditions.
- 2: Set the parameters of the design method, including population size N_P , the maximum number of iterations G_{max} and parameters related to offspring generation.
- 3: Set $G = 1$; G stands for the current generation number.
- 4: Randomly generate the parent population P_0 consisting of N_P antenna arrangements.
- 5: Interpret the individuals by discretization(trait expression). Manifest the individuals as antenna arrangements according to (20).
- 6: Employ the mutant operator *DE-rand-1* and the binomial crossover operator to generate offspring population O_G . Regenerate the antenna arrangement if it violates the boundary constraints after evolution.
- 7: Calculate the objective function and the constraint violations of O_G and P_{G-1} . Compare O_G with P_{G-1} pairwise. Choose the better antenna arrangements according to the feasibility rule to form P_G .
- 8: **if** stopping criterion is satisfied **then**
- 9: Stop and output the final population P_G as the sensing matrix design results.
- 10: **else**
- 11: $G = G + 1$ and go to step 5.
- 12: **end if**

integer variable β_j , which indicates whether the j th position should be mounted with an antenna element. Discretization reveals how an individual manifest as an antenna arrangement, which can be formulated as

$$\beta_{j,i} = d_i(x_{j,i}) \quad (20)$$

where $\beta_{j,i}$ represents the j th trait of the i th individual, $x_{j,i}$ represents the j th real variable (gene) of the i th individual, and $d_i(x_{j,i})$ represents the i th discretization function. For simplicity, we set $d_i(x_{j,i}) = [x_{j,i}]$, $\forall i$, where $[\cdot]$ presents the rounding operator. After discretization, the antenna arrangement's performance can be evaluated by calculating its objective function and its constraint violation.

Offspring is generated by evolution, which includes two procedures: mutation and crossover. The mutation operator *DE-rand-1* [60] is employed to create a mutant vector for each individual

$$\vec{v}_i = \vec{x}_{r_1^i} + F \cdot (\vec{x}_{r_2^i} - \vec{x}_{r_3^i}) \quad (21)$$

where \vec{v}_i is the mutant vector, the indices r_1 , r_2 , and r_3 are three mutually different integers randomly selected from $[1, N_P]$, which are also different from the base vector index i , and F is the mutation parameter.

If one individual violates the boundary constraints after mutation, it is randomly regenerated. Then, the binomial crossover is employed to generate the trial vector \vec{u}_i , whose variable can be formulated as

$$u_{j,i} = \begin{cases} v_{j,i}, & \text{if } (\text{rand}_{j,i}[0, 1] \leq Cr \text{ or } j = j_{\text{rand}}) \\ x_{j,i}, & \text{otherwise} \end{cases} \quad (22)$$

TABLE I
DESIGN PARAMETERS

	Parameter	Symbol	Value
System Parameter	Wavelength(m)	λ	0.03
	Range from the antenna array center to the scene center (m)	R_{R0}	2000
	The total number of positions for mounting antenna elements	N_C	2001
	Spacing between adjacent positions(m)	d	0.015
	The number of optional positions on a UAV	l	60
	The number of unavailable positions between adjacent UAVs	m	40
Algorithm Parameter	Mutation scalar number	F	0.5
	Crossover rate	Cr	0.9
	Population number	N_P	100
	The maximum iteration	G_{max}	800
	Threshold	ε	0.0001

where Cr is called the crossover rate and j_{rand} is a randomly chosen index.

After evolution, the feasibility rule in [61] is employed for offspring selection, which puts the emphasis on feasibility and, therefore, motivates the population to approach the feasible region promptly. Then, check whether $|(\min_x f(x_G) - \min_x f(x_{G-1}))| < \varepsilon$ or $G \geq G_{max}$, where $\min_x f(x_G)$ represents the minimum objective function in P_G . If the difference between the minimum objective function of the current generation and that of the previous generation is less than the threshold ε , or the current generation number is equal to the maximum number of iterations, stop and output the final population.

In this section, a sensing matrix design method based on DCDE is proposed. DCDE can be used to solve discrete integer programming problems, such as sensing matrix design problems efficiently. In the proposed method, the discretization function is designed to translate genes into traits, which reveals how to decide whether a position should be mounted with an antenna element. Therefore, individuals can evolve in the continuous decision space with great diversity, while traits still perform in the discrete decision space.

V. SIMULATION RESULTS

Simulations are carried out in this section to illustrate the effectiveness of our proposed method. First, a simulation of a range slice is carried out. Imaging results obtained using the uniform configuration, random configuration, and optimized configuration are used for comparison. Furthermore, the grating lobe phenomenon is analyzed. Then, a 3-D image target simulation and a 3-D terrain scene simulation are presented.

As listed in Table I, the wavelength of the transmitting signal λ is 0.03 m, the range from the antenna array center

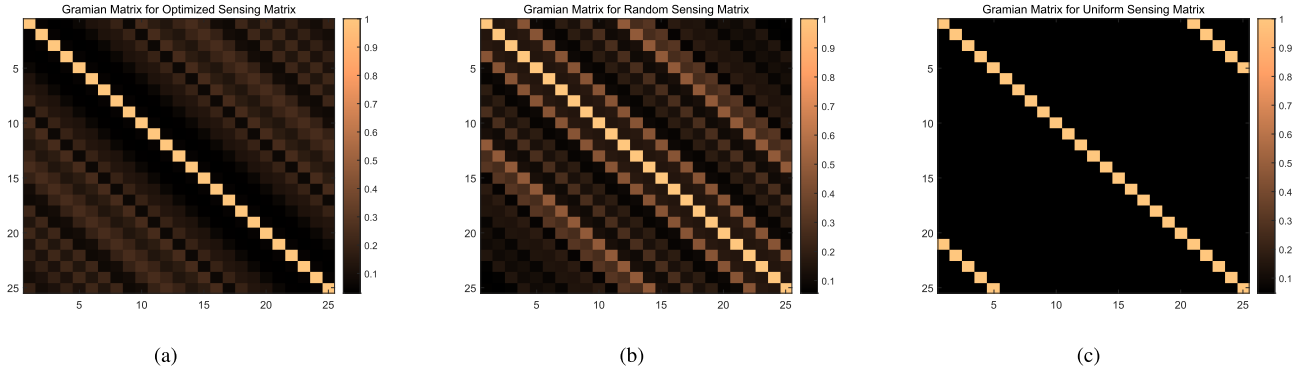


Fig. 7. Gramian matrices of different sensing matrices in simulation A. (a) Optimized configuration. (b) Random configuration. (c) Uniform configuration.

to the scene center R_{R0} is 2000 m, the array's width L_c is 30 m, the total number of positions N_C is set to 2001, and the spacing between adjacent positions d is 0.015 m. Besides, the number of optional positions on a UAV platform l is set to 60, and the number of unavailable positions between adjacent UAVs m is set to 40. The mutation scalar number F is set to 0.5, the crossover rate Cr is set to 0.9, the threshold ε is set to 0.0001, the number of the genomes N_P is set to 100, and the maximum generation G_{\max} is set to 800. In each simulation, the cross-track Gramian matrices $Gr = F_S^H F_S$ of the sensing matrices obtained with different configurations are presented and analyzed, which reveal the correlation coefficient of different configurations. Moreover, the reconstruction images of the range slices or 3-D target scenes obtained using different configurations are compared. Last but not least, two evaluation indices, i.e., the peak signal-to-noise ratio (PSNR) and the structure similarity (SSIM), are utilized to analyze the reconstruction quality.

A. Range Slice Simulation

In this section, 21 antenna elements are utilized to observe a range slice where 24 point targets are distributed. Fig. 7(a)–(c) displays the magnitude of the Gramian matrices of the normalized sensing matrices with the optimized, uniform, and random antenna arrangement, respectively. The Gramian matrix can be regarded as a focusing operation. Therefore, its off-diagonal maximum magnitude measures the absolute value of the largest sidelobe over all focusing positions, which can be used to assess the focusing capabilities of imaging systems [39]. We can infer intuitively that the correlation coefficient of the optimized configuration is the lowest. In Fig. 7(a), the color of the off-diagonal elements is basically black, and the color changes gently between adjacent pixels. The correlation coefficient of the optimized configuration is around 0.25. On contrary, in Fig. 7(b), the color changes significantly, and the correlation coefficient of the random configuration is around 0.5. In Fig. 7(c), the grating lobe phenomenon is discovered. There are ten off-diagonal elements in Fig. 7(c), which have the same color as the diagonal elements, demonstrating that the correlation coefficient of the uniform configuration is 1. To further analyze the grating lobe phenomenon,

the ambiguity function of the uniform configuration is given as follows:

$$\begin{aligned} & |\chi_C(\Delta R(P_i, P_j))| \\ &= \frac{1}{N_C} \left| \sum_{k=1}^{N_C} \exp \left(-j K_0 \frac{d'(k-1)(y_j - y_i)}{R_{R0}} \right) \right| \\ &= \left| \frac{\sin \left(\frac{K_0 d' N_C (y_j - y_i)}{2 R_{R0}} \right)}{N_C \sin \left(\frac{K_0 d' (y_j - y_i)}{2 R_{R0}} \right)} \right|. \end{aligned} \quad (23)$$

According to (23), when $((K_0 d' (y_j - y_i)) / (2 R_{R0})) = k\pi$, the value of the ambiguity function is 1. Therefore, the larger the spacing between adjacent antenna d' is, the closer the grating lobe is to the main lobe. In the uniform configuration of simulation A, the spacing between adjacent antenna d' is 1.5 m, and the grating lobe appears when the interval is 40 m in the cross-track direction. Because of the grating lobes, it is incapable to distinguish two scattering points 40 m apart in the uniform configuration, which is unacceptable in real-world applications.

By observing the reconstructed images, the superiority of the optimized configuration is revealed more intuitively. Fig. 8(a) displays the true scalar backscattering coefficient vector with 24 nonzero values. Fig. 8(b)–(d) displays the reconstructed vector obtained by OMP [62], a classic reconstruction algorithm, using the optimized, random, and uniform configurations, respectively. As depicted in the figures, the sparse backscattering coefficient vector is recovered exactly using the optimized configuration. On contrary, reconstruction using the uniform configuration faces the problem of grating lobes, which results in the wrong positions of the scatterers, and reconstruction using the random configuration suffers from significant errors in both the magnitudes of the backscattering coefficient value and the positions of the scatterers. In Fig. 8(d) where the uniform configuration is used for recovery, two scattering points are located in the wrong positions with the correct backscattering coefficient, which may mislead the image interpretation and cause serious consequences.

To quantitatively illustrate the benefits of the proposed design method, we introduce PSNR and SSIM to analyze the

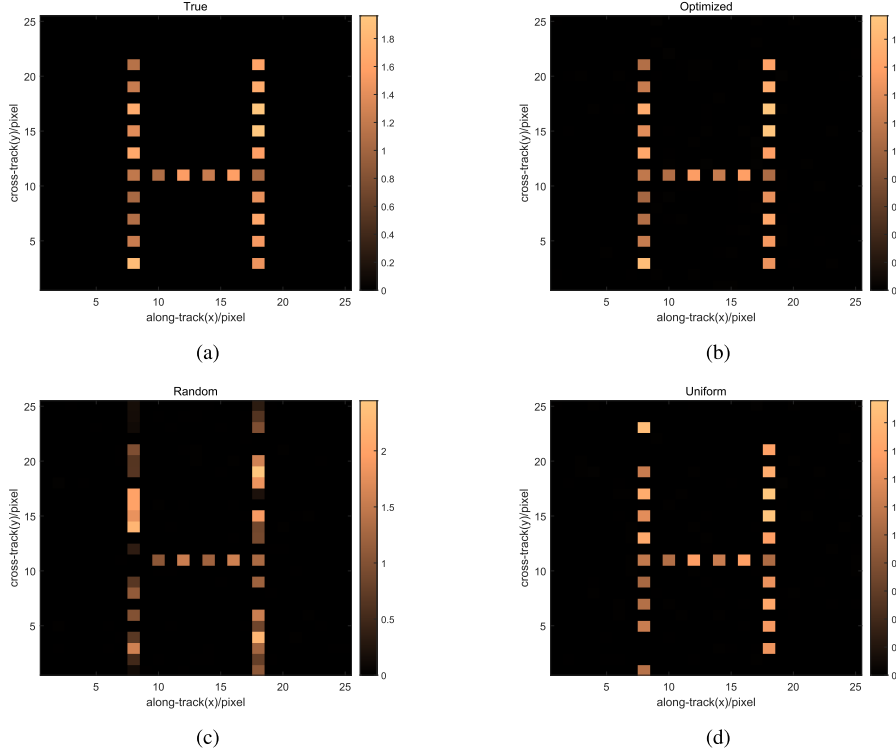


Fig. 8. Imaging results of a range slice. (a) True image. (b) Image recovered by OMP using optimized antenna arrangement. (c) Image recovered by OMP using random antenna arrangement. (d) Image recovered by OMP using uniform antenna arrangement.

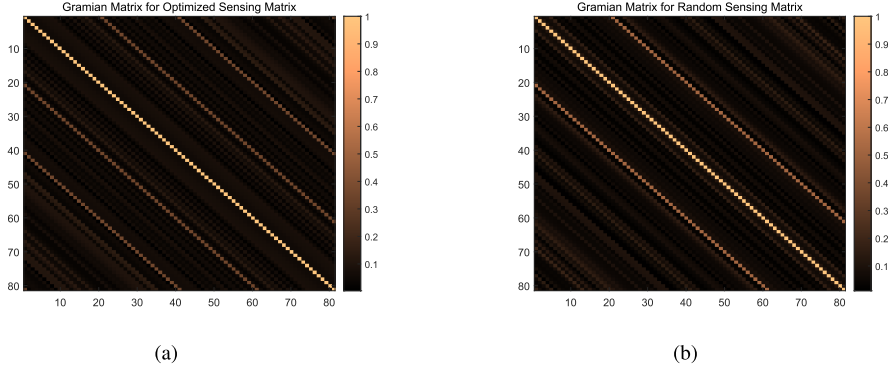


Fig. 9. Gramian matrices of different sensing matrices in simulations B and C. (a) Optimized configuration. (b) Random configuration.

reconstruction quality of the whole image. PSNR is a classic measure of image quality, which can be calculated by

$$\text{PSNR} = 20\log_{10}\left(\frac{\max|\Gamma_{\text{or}}|}{\text{RMSE}}\right). \quad (24)$$

Note that RMSE is the root mean square error of the recovered image and can be calculated by

$$\text{RMSE} = \sqrt{\frac{1}{n}\|\Gamma_{\text{or}} - \Gamma_{\text{re}}\|_F^2} \quad (25)$$

where Γ_{or} and Γ_{re} denote the original reflectivity coefficients and the recovered reflectivity coefficients of the SAR image, respectively, and n denotes the number of the pixels. A larger PSNR means better reconstruction performance.

SSIM is a measure of the similarity between two images. Given two images x and y , SSIM can be calculated by

$$\text{SSIM}(x, y) = \frac{(2\mu_x\mu_y + c_1)(2\sigma_{xy} + c_2)}{(\mu_x^2 + \mu_y^2 + c_1)(\sigma_x^2 + \sigma_y^2 + c_2)} \quad (26)$$

where x is the original image, y is the reconstructed image, μ_x and μ_y denote the mean of x and y , respectively, σ_x^2 and σ_y^2 denote the variance of x and y , respectively, σ_{xy} is the covariance between x and y , and c_1 and c_2 are constants used to maintain stability. The closer the SSIM value is to 1, the higher the similarity between x and y .

The PSNR and SSIM values of the final images obtained by different designs in simulation A are listed in Table II. It can be found that the PSNR value of the image obtained by optimized design is higher than 40 dB, indicating that the

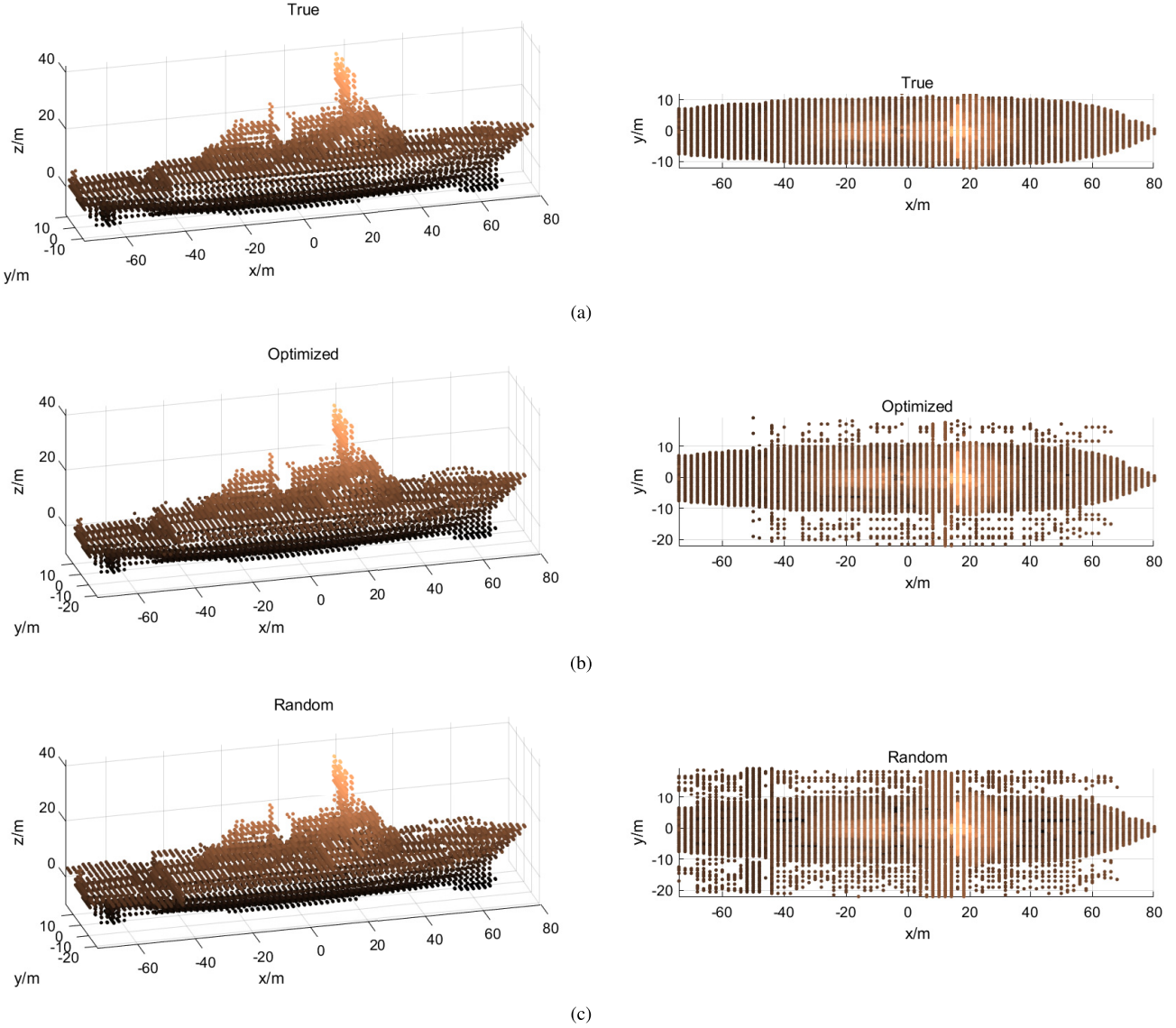


Fig. 10. Imaging results of a 3-D target. (Left) 3-D view of the images. (Right) Top view (XY plane) of the images. (a) Original image of a vessel. (b) Image recovered by OMP using optimized antenna arrangement. (c) Image recovered by OMP using random antenna arrangement.

TABLE II

PSNR AND SSIM VALUES OF THE FINAL IMAGES OBTAINED BY DIFFERENT DESIGNS IN SIMULATION A

Simulation A	Optimized design	Random design	Uniform design
PSNR	43.99dB	11.20dB	18.21dB
SSIM	0.9832	0.6026	0.8432

recovered image is very close to the original image. On the contrary, the PSNR values of the images obtained by random design and uniform design are lower than 20 dB, indicating that the image quality is unacceptable. The SSIM values show that the image obtained by the optimized design has the highest similarity to the original image.

B. 3-D Target Simulation

In this section, 101 antenna elements are utilized to observe a 3-D target scene. Since the uniform antenna arrangement

does not meet the spacing constraint, we only compare the simulation results of optimized and random antenna arrangements. Fig. 9(a) and (b) displays the magnitude of the Gramian matrices of the normalized sensing matrices with the optimized and random antenna arrangements, respectively. Like in the previous example, it is clearly visible that the correlation coefficient of the optimized configuration is the lowest. In Fig. 9(a), the color of the off-diagonal elements is basically black, and the correlation coefficient of the optimized configuration is around 0.35. On the contrary, in Fig. 9(b), the correlation coefficient of the random configuration is around 0.52.

The difference in reconstruction accuracy between optimized and random configurations can be revealed visually by inspecting the reconstructed images. Fig. 10(a) displays the original 3-D image of a vessel, and Fig. 10(b) and (c) displays the reconstructed results obtained by OMP using the optimized and random antenna positions, respectively. Fig. 11(a) displays the true images of two slices of the target scene,

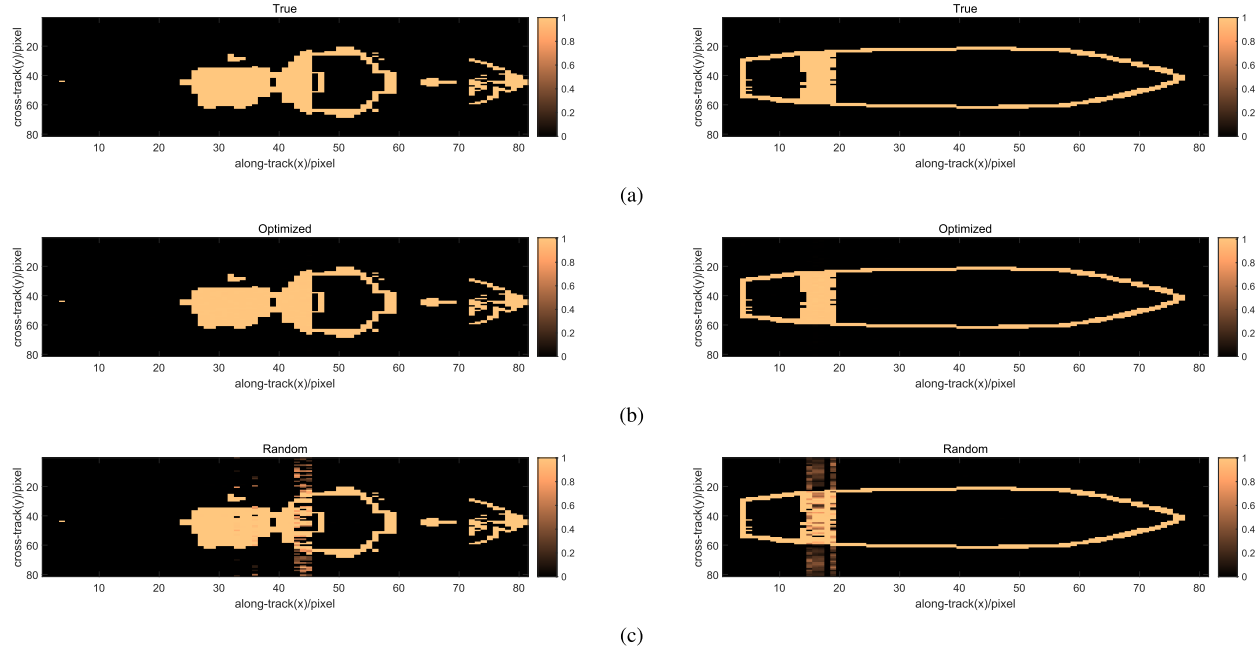


Fig. 11. Imaging results of different slices. (Left) Slice 1. (Right) Slice 2. (a) Original images of two different slices. (b) Images recovered by OMP using optimized antenna arrangement. (c) Images recovered by OMP using random antenna arrangement.

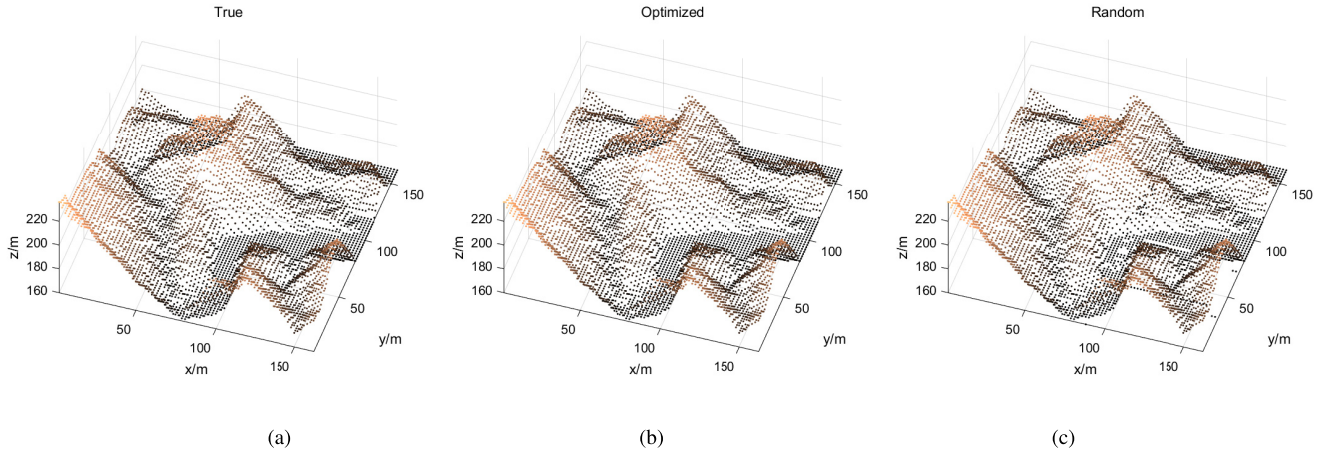


Fig. 12. Imaging results of a 3-D terrain. (a) Original terrain image. (b) Image recovered by OMP using optimized antenna arrangement. (c) Image recovered by OMP using random antenna arrangement.

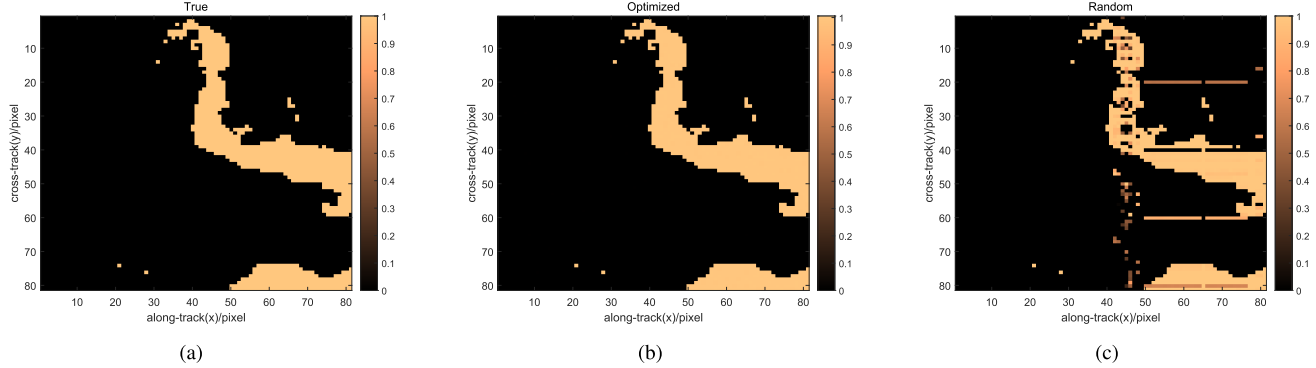


Fig. 13. Imaging results of range slice 1. (a) Original image. (b) Image recovered by OMP using optimized antenna arrangement. (c) Image recovered by OMP using random antenna arrangement.

and Fig. 11(b) and (c) displays the reconstructed results of these two slices obtained by OMP using the optimized

and random configurations, respectively. It can be concluded from Fig. 10 that the optimized configuration can

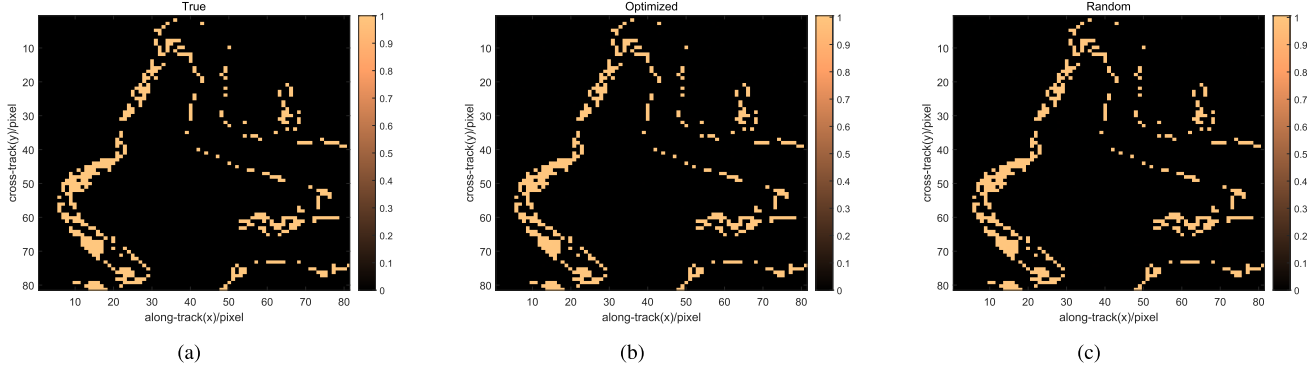


Fig. 14. Imaging results of range slice 2. (a) Original image. (b) Image recovered by OMP using optimized antenna arrangement. (c) Image recovered by OMP using random antenna arrangement.

TABLE III

PSNR AND SSIM VALUES OF THE RECOVERED SLICES OBTAINED BY DIFFERENT DESIGNS IN SIMULATION B

Simulation B	Optimized design	Random design
Slice1	PSNR	61.58dB
	SSIM	0.9994
Slice2	PSNR	55.82dB
	SSIM	0.9963

TABLE IV

PSNR AND SSIM VALUES OF THE RECOVERED SLICES OBTAINED BY DIFFERENT DESIGNS IN SIMULATION C

Simulation C	Optimized design	Random design
Slice1	PSNR	63.01dB
	SSIM	0.9998
Slice2	PSNR	62.05dB
	SSIM	0.9996

C. 3-D Terrain Simulation

generate more accurate 3-D reconstruction images than the random configuration. Inspecting the top view (XY plane) of the reconstruction image, we can clearly discover that there are fewer fake scattering points around the real target using the optimized configuration. As can be seen from Fig. 11, the along-track pixels can be recovered exactly using either the optimized configuration or the random configuration since the along-track ambiguity function is not affected by the position distribution of the antenna elements. However, for cross-track pixels, only by using the optimized configuration can the sparse backscattering coefficient vector be accurately recovered, while the reconstruction using the random configuration suffer from significant errors in both the magnitudes of the backscattering coefficient value and the positions of the scatterers. Strong scattering points generated by incorrect reconstruction in Fig. 11(c) dim the overall color of the image, which results in difficulty to distinguish the detail.

The PSNR and SSIM values of the recovered slices obtained by different designs in simulation B are listed in Table III. We can observe that the PSNR values of slice1 and slice2 obtained by optimized design are 61.58 and 55.82 dB, respectively, indicating excellent image quality. On the contrary, the PSNR values of slice1 and slice2 obtained by random design are 19.62 and 21.77 dB, respectively, indicating poor image quality. The SSIM values also demonstrate that images obtained by optimized design have higher similarity to the original images.

In this section, 101 antenna elements are utilized to observe a 3-D target scene. Since the uniform antenna arrangement does not meet the spacing constraint, we only compare the simulation results of optimized and random antenna arrangements. The magnitude of the Gramian matrices of the normalized sensing matrices with the optimized and random configurations keeps the same as the magnitude of the Gramian matrices in Section V-B. Fig. 12(a) displays the original 3-D image of terrain, and Fig. 12(b) and (c) displays the reconstructed results obtained by OMP using the optimized and random antenna positions, respectively. Figs. 13 and 14 display the true images of two range slices of the 3-D terrain scene and the corresponding reconstructed results obtained by OMP using the optimized and random antenna positions, respectively. As can be seen from Fig. 12, the optimized configuration can generate more accurate 3-D reconstruction images than the random configuration. For the range slice depicted in Fig. 14, the image can be accurately recovered using both the optimized configuration and the random configuration since the scattering points are quite sparse in range slice 2. However, as for the range slice depicted in Fig. 13, the scattering points are closely distributed. In that case, only the optimized configuration can obtain the satisfying reconstruction result.

The PSNR and SSIM values of the recovered slices obtained by different designs in simulation C are listed in Table IV. As we can see, both optimized design and random design can recover a high-quality image of slice 2 with PSNR higher than 60 dB and SSIM close to 1. However, as for slice 1, the PSNR

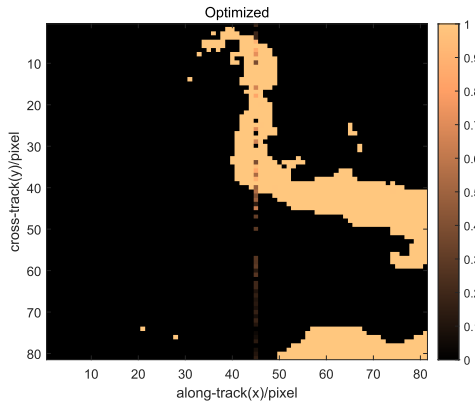


Fig. 15. Reconstruction results obtained by optimized antenna arrangement under perturbation.

TABLE V
PSNR AND SSIM VALUES (MEAN AND STD) AND THE SUCCESS RATE ON EACH SET OF PERTURBATION SIMULATIONS

Simulation D	PSNR(Mean+STD)	SSIM(Mean+STD)	Success Rate
0cm	63.47dB(0.19)	0.9998(2.77e-5)	100%
5cm	61.53dB(9.53)	0.9963(1.58e-2)	95%
10cm	61.32dB(9.47)	0.9963(1.57e-2)	95%
15cm	47.94dB(19.71)	0.9783(2.81e-2)	60%
20cm	45.90dB(19.88)	0.9768(2.66e-2)	55%

value of the image recovered by optimized design is 63.01 dB, and the SSIM value is 0.9998, while the PSNR value of the image recovered by random design is 17.22 dB, and the SSIM value is 0.8132. Therefore, it can be concluded that using the optimized design can obtain the recovered image with better performance.

D. Perturbation Analysis

In practical applications, the UAV position will be affected by many other environmental disturbances and cannot satisfy the matrix design completely. However, under certain control schemes, the disturbances can be attenuated or even eliminated [63]. In this section, random Gaussian position errors of different standard deviations (20, 15, 10, 5, and 0 cm, respectively) are introduced in five sets of simulations, and accordingly, and the optimized antenna arrangement is perturbed. In each set, the reconstruction results of slice1 in Section V-C obtained by optimized antenna arrangement under random perturbations of different standard deviations are analyzed. Table V presents the PSNR and SSIM values (mean and standard deviation) over 20 independent runs on each set of simulations. Moreover, Table V also provides the success rates of complete reconstruction. It can be found from the table that the reconstruction performance gradually deteriorates with the increase in the standard deviation of random perturbation. Nevertheless, even when the standard deviation of random perturbation is 20 cm, the perturbed optimized antenna arrangement can still fully reconstruct the image in 55% of cases. In the remaining 45% of cases, the matrix can also reconstruct the image to a large extent, as depicted in Fig. 15.

VI. CONCLUSION

In this article, the swarm UAV SAR system is first proposed. The system concept of the swarm UAV SAR system is explained, and the motivations and advantages of the system are analyzed specifically. Moreover, three missions of the swarm UAV SAR system, including simultaneous multispect observation, multifrequency observation, and 3-D imaging, are introduced. Afterward, the swarm UAV 3-D LASAR system is proposed, where sparse LASAR is combined with the swarm UAV SAR system. The system is capable of forward-looking 3-D imaging and has a better cross-track resolution. CS theory is utilized for 3-D imaging, thus greatly reducing the cost of data storage, transmission, and processing. The signal model of the swarm UAV 3-D LASAR is established, and the sensing matrix is given. Then, the derivation of the correlation coefficient of the sensing matrix is described elaborately. The relationship between the reconstruction performance and the position distribution of the antenna elements is analyzed. The mission design for the swarm UAV 3-D SAR aims at finding an optimal distribution of the antenna elements to obtain the best reconstruction performance. The mission design is modeled as a constraint single-objective optimization problem. Finally, a sensing matrix design method based on the DCDE algorithm is proposed for solving the optimization problem, whose procedures are explained in detail. Experimental results have verified the effectiveness of our proposed method.

REFERENCES

- [1] A. Moreira, P. Prats-Iraola, M. Younis, G. Krieger, and I. Hajnsek, "A tutorial on synthetic aperture radar," *IEEE Geosci. Remote Sens. Mag.*, vol. 1, no. 1, pp. 6–43, Mar. 2013.
- [2] Z. Li, J. Wu, Y. Huang, Z. Sun, and J. Yang, "Ground-moving target imaging and velocity estimation based on mismatched compression for bistatic forward-looking SAR," *IEEE Trans. Geosci. Remote Sens.*, vol. 54, no. 6, pp. 3277–3291, Jan. 2016.
- [3] E. Schreiber, A. Heinzel, M. Peichl, M. Engel, and W. Wiesbeck, "Advanced buried object detection by multichannel, UAV/drone carried synthetic aperture radar," in *Proc. 13th EUCAP*, 2019, pp. 1–5.
- [4] A. Bekar, M. Antoniou, and C. J. Baker, "Low-cost, high-resolution, drone-borne SAR imaging," *IEEE Trans. Geosci. Remote Sens.*, vol. 60, pp. 1–11, 2022.
- [5] Y. A. Su, W. Liu, H. Feng, and B. P. Ng, "Study of multi-rotor UAV SAR processing," in *Proc. IEEE Radar Conf. (RadarConf)*, May 2017, pp. 226–232.
- [6] M.-L. Ding, C.-B. Ding, L. Tang, X.-M. Wang, J.-M. Qu, and R. Wu, "A W-band 3-D integrated mini-SAR system with high imaging resolution on UAV platform," *IEEE Access*, vol. 8, pp. 113601–113609, 2020.
- [7] M. Fernández et al., "Synthetic aperture radar imaging system for landmine detection using a ground penetrating radar on board a unmanned aerial vehicle," *IEEE Access*, vol. 6, pp. 45100–45112, 2018.
- [8] O. O. Bezvesilniy, I. M. Gorovyi, and D. M. Vavriv, "Estimation of phase errors in SAR data by local-quadratic map-drift autofocus," in *Proc. 13th Int. Radar Symp.*, May 2012, pp. 376–381.
- [9] O. O. Bezvesilniy, I. M. Gorovyi, and D. M. Vavriv, "Autofocusing SAR images via local estimates of flight trajectory," *Int. J. Microw. Wireless Technol.*, vol. 8, no. 6, pp. 881–889, Sep. 2016.
- [10] I. M. Gorovyi, O. O. Bezvesilniy, and D. M. Vavriv, "A novel trajectory restoration algorithm for high-resolution SAR imaging," in *Proc. 15th Int. Radar Symp. (IRS)*, Jun. 2014, pp. 1–4.
- [11] Z. Sun, J. Wu, J. Yang, Y. Huang, C. Li, and D. Li, "Path planning for GEO-UAV bistatic SAR using constrained adaptive multiobjective differential evolution," *IEEE Trans. Geosci. Remote Sens.*, vol. 54, no. 11, pp. 1–14, Nov. 2016.
- [12] Z. Sun, G. G. Yen, J. Wu, H. Ren, H. An, and J. Yang, "Mission planning for energy-efficient passive UAV radar imaging system based on substage division collaborative search," *IEEE Trans. Cybern.*, early access, Aug. 3, 2021, doi: 10.1109/TCYB.2021.3090662.

- [13] M. Chen, H. Wang, C.-Y. Chang, and X. Wei, "SIDR: A swarm intelligence-based damage-resilient mechanism for UAV swarm networks," *IEEE Access*, vol. 8, pp. 77089–77105, 2020.
- [14] Y. Zhou, B. Rao, and W. Wang, "UAV swarm intelligence: Recent advances and future trends," *IEEE Access*, vol. 8, pp. 183856–183878, 2020.
- [15] F. Santi, M. Antoniou, and D. Pastina, "Point spread function analysis for GNSS-based multistatic SAR," *IEEE Geosci. Remote Sens. Lett.*, vol. 12, no. 2, pp. 304–308, Feb. 2015.
- [16] C. Hu, Z. Chen, X. Dong, and C. Cui, "Multistatic geosynchronous SAR resolution analysis and grating lobe suppression based on array spatial ambiguity function," *IEEE Trans. Geosci. Remote Sens.*, vol. 58, no. 9, pp. 6020–6038, Sep. 2020.
- [17] Z. Sun, J. Wu, Y. Huang, J. Yang, H. Yang, and X. Yang, "Performance analysis and mission design for inclined geosynchronous spaceborne-airborne bistatic SAR," in *Proc. IEEE Radar Conf.*, May 2015, pp. 1177–1181.
- [18] H. An, J. Wu, Z. Sun, J. Yang, Y. Huang, and H. Yang, "Topology design for geosynchronous spaceborne-airborne multistatic SAR," *IEEE Geosci. Remote Sens. Lett.*, vol. 15, no. 11, pp. 1715–1719, Nov. 2018.
- [19] F. Behner, S. Reuter, H. Nies, and O. Loffeld, "Synchronization and processing in the HITCHHIKER bistatic SAR experiment," *IEEE J. Sel. Topics Appl. Earth Observ. Remote Sens.*, vol. 9, no. 3, pp. 1028–1035, Mar. 2015.
- [20] I. Stojanovic and W. C. Karl, "Imaging of moving targets with multistatic SAR using an overcomplete dictionary," *IEEE J. Sel. Topics Signal Process.*, vol. 4, no. 1, pp. 164–176, Feb. 2010.
- [21] M. Liu, P. Wang, and Z. Wang, "3D velocity estimation based on FrFT for multi-static SAR," *Electron. Lett.*, vol. 52, no. 18, pp. 1565–1567, Sep. 2016.
- [22] I. Walterscheid and A. R. Brenner, "Multistatic and multi-aspect SAR data acquisition to improve image interpretation," in *Proc. IEEE Int. Geosci. Remote Sens. Symp.*, Jul. 2013, pp. 4194–4197.
- [23] E. H. Peterson, G. Fotopoulos, A. Schmitt, R. E. Zee, and A. Roth, "Registration of multi-frequency SAR imagery using phase correlation methods," in *Proc. IEEE Int. Geosci. Remote Sens. Symp.*, Jul. 2011, pp. 3708–3711.
- [24] F. Lombardini, F. Cai, and D. Pasculli, "Spaceborne 3-D SAR tomography for analyzing garbled urban scenarios: Single-look superresolution advances and experiments," *IEEE J. Sel. Topics Appl. Earth Observ. Remote Sens.*, vol. 6, no. 2, pp. 960–968, Apr. 2013.
- [25] A. Aljurbua and K. Sarabandi, "Detection and localization of buried pipelines using a 3-D multistatic imaging radar," *IEEE Trans. Geosci. Remote Sens.*, vol. 60, pp. 1–10, 2022.
- [26] L. Chen, X. Jiang, Z. Li, X. Liu, and Z. Zhou, "Feature-enhanced speckle reduction via low-rank and space-angle continuity for circular SAR target recognition," *IEEE Trans. Geosci. Remote Sens.*, vol. 58, no. 1, pp. 7734–7752, Nov. 2020.
- [27] A. Ishimaru, T.-K. Chan, and Y. Kuga, "An imaging technique using confocal circular synthetic aperture radar," *IEEE Trans. Geosci. Remote Sens.*, vol. 36, no. 5, pp. 1524–1530, Sep. 1998.
- [28] T.-K. Chan, Y. Kuga, and A. Ishimaru, "Experimental studies on circular SAR imaging in clutter using angular correlation function technique," *IEEE Trans. Geosci. Remote Sens.*, vol. 37, no. 5, pp. 2192–2197, Sep. 1999.
- [29] Z. Su, Y. Peng, and X. Wang, "Feature-independent aperture evaluator for the curvilinear SAR," *IEEE Geosci. Remote Sens. Lett.*, vol. 4, no. 2, pp. 191–195, Apr. 2007.
- [30] O. Ponce, P. Prats, M. Rodriguez-Cassola, R. Scheiber, and A. Reigber, "Processing of circular SAR trajectories with fast factorized back-projection," in *Proc. IEEE Int. Geosci. Remote Sens. Symp.*, Jul. 2011, pp. 3692–3695.
- [31] D. Reale, G. Fornaro, A. Pauciullo, X. Zhu, and R. Bamler, "Tomographic imaging and monitoring of buildings with very high resolution SAR data," *IEEE Geosci. Remote Sens. Lett.*, vol. 8, no. 4, pp. 661–665, Jul. 2011.
- [32] X. X. Zhu and R. Bamler, "Demonstration of super-resolution for tomographic SAR imaging in urban environment," *IEEE Trans. Geosci. Remote Sens.*, vol. 50, no. 8, pp. 3150–3157, Aug. 2012.
- [33] O. Frey and E. Meier, "Analyzing tomographic SAR data of a forest with respect to frequency, polarization, and focusing technique," *IEEE Trans. Geosci. Remote Sens.*, vol. 49, no. 10, pp. 3648–3659, Oct. 2011.
- [34] S. Zhang, G. Dong, and G. Kuang, "Matrix completion for downward-looking 3-D SAR imaging with a random sparse linear array," *IEEE Trans. Geosci. Remote Sens.*, vol. 56, no. 4, pp. 1994–2006, Apr. 2018.
- [35] C. H. Gierull, "On a concept for an airborne downward-looking imaging radar," *AEU-Int. J. Electron. Commun.*, vol. 53, no. 6, pp. 295–304, 1999.
- [36] M. Weiss and M. Gilles, "Initial ARTINO radar experiments," in *Proc. 8th EUSAR*, 2010, pp. 1–4.
- [37] E. J. Candès, J. Romberg, and T. Tao, "Robust uncertainty principles: Exact signal reconstruction from highly incomplete frequency information," *IEEE Trans. Inf. Theory*, vol. 52, no. 2, pp. 489–509, Feb. 2006.
- [38] D. L. Donoho, "Compressed sensing," *IEEE Trans. Inf. Theory*, vol. 52, no. 4, pp. 1289–1306, Apr. 2006.
- [39] R. Obermeier and J. A. Martinez-Lorenzo, "Sensing matrix design via mutual coherence minimization for electromagnetic compressive imaging applications," *IEEE Trans. Comput. Imag.*, vol. 3, no. 2, pp. 217–229, Jun. 2017.
- [40] Q. Bao, C. Jiang, Y. Lin, W. Tan, Z. Wang, and W. Hong, "Measurement matrix optimization and mismatch problem compensation for DLSLA 3-D SAR cross-track reconstruction," *Sensors*, vol. 16, no. 8, p. 1333, Aug. 2016.
- [41] C. Lu, H. Li, and Z. Lin, "Optimized projections for compressed sensing via direct mutual coherence minimization," *Signal Process.*, vol. 151, pp. 45–55, Oct. 2018.
- [42] P. Runkle, L. H. Nguyen, J. H. McClellan, and L. Carin, "Multi-aspect target detection for SAR imagery using hidden Markov models," *IEEE Trans. Geosci. Remote Sens.*, vol. 39, no. 1, pp. 46–55, Jan. 2001.
- [43] S. Papson and R. M. Narayanan, "Classification via the shadow region in SAR imagery," *IEEE Trans. Aerosp. Electron. Syst.*, vol. 48, no. 2, pp. 969–980, Apr. 2012.
- [44] H. Zhang, M. Nasser, and Y. Zhang, "Multi-view automatic target recognition using joint sparse representation," *IEEE Trans. Aerosp. Electron. Syst.*, vol. 48, no. 3, pp. 2481–2497, Jul. 2012.
- [45] Z. Sun, J. Wu, J. Pei, Z. Li, Y. Huang, and J. Yang, "Inclined geosynchronous spaceborne-airborne bistatic SAR: Performance analysis and mission design," *IEEE Trans. Geosci. Remote Sens.*, vol. 54, no. 1, pp. 343–357, Jan. 2016.
- [46] T. Li et al., "A mean field game-theoretic cross-layer optimization for multi-hop swarm UAV communications," *J. Commun. Netw.*, vol. 24, no. 1, pp. 68–82, 2022.
- [47] Y. Zhang, S. Chang, R. Wang, and Y. Deng, "An innovative push-to-talk (PTT) synchronization scheme for distributed SAR," *IEEE Trans. Geosci. Remote Sens.*, vol. 60, pp. 1–13, 2022.
- [48] X. Dong, Y. Li, C. Lu, G. Hu, Q. Li, and Z. Ren, "Time-varying formation tracking for UAV swarm systems with switching directed topologies," *IEEE Trans. Neural Netw. Learn. Syst.*, vol. 30, no. 12, pp. 3674–3685, Dec. 2019.
- [49] G. Jing, H. Wang, M. Xing, and X. Lin, "A novel two-step registration method for multi-aspect SAR images," in *Proc. CISS*, 2018, pp. 1–4.
- [50] Y. L. Li, X. D. Liang, L. J. Zhou, L. Y. Chen, and C. B. Ding, "Introduction to IECAS-SAR—A multi-frequency polarimetric airborne SAR," in *Proc. Geosci. Remote Sens. Symp.*, 2014, pp. 1085–1088.
- [51] R. L. Jordan, B. L. Huneycutt, and M. Werner, "The SIR-C/X-SAR synthetic aperture radar system," *Proc. IEEE*, vol. 79, no. 6, pp. 827–838, Jun. 1991.
- [52] L. Van Hove, "Correlations in space and time and born approximation scattering in systems of interacting particles," *Phys. Rev.*, vol. 95, no. 1, pp. 249–262, Jul. 1954.
- [53] S.-J. Wei, X.-L. Zhang, and J. Shi, "Linear array SAR imaging via compressed sensing," *Prog. Electromagn. Res.*, vol. 117, pp. 299–319, 2011.
- [54] C. Li, J. Gao, T. Zhang, and X. Wang, "Differential evolution algorithm for constraint joint replenishment problem with indirect grouping strategy," *Int. J. Hybrid Inf. Technol.*, vol. 8, no. 5, pp. 259–266, May 2015.
- [55] B. A. Foster and D. M. Ryan, "An integer programming approach to the vehicle scheduling problem," *Oper. Res. Quart.*, vol. 27, no. 2, p. 367, 1976.
- [56] E. L. Lawler and D. E. Wood, "Branch-and-bound methods: A survey," *Oper. Res.*, vol. 14, no. 4, pp. 699–719, Jul./Aug. 1966.
- [57] J. E. Mitchell and B. Borchers, "Solving real-world linear ordering problems using a primal-dual interior point cutting plane method," *Ann. Oper. Res.*, vol. 62, no. 1, pp. 253–276, Dec. 1996.
- [58] R. Romero and A. Monticelli, "A zero-one implicit enumeration method for optimizing investments in transmission expansion planning," *IEEE Trans. Power Syst.*, vol. 9, no. 3, pp. 1385–1391, Aug. 1994.
- [59] Z. Sun et al., "An evolutionary algorithm with constraint relaxation strategy for highly constrained multiobjective optimization," *IEEE Trans. Cybern.*, early access, Mar. 11, 2022, doi: [10.1109/TCYB.2022.3151974](https://doi.org/10.1109/TCYB.2022.3151974).

- [60] S. Das and P. N. Suganthan, "Differential evolution: A survey of the state-of-the-art," *IEEE Trans. Evol. Comput.*, vol. 15, no. 1, pp. 4–31, Feb. 2011.
- [61] Z. Fan, L. Hui, C. Wei, W. Li, and Z. Cai, "An improved epsilon constraint handling method embedded in MOEA/D for constrained multi-objective optimization problems," in *Proc. IEEE SSCI*, Mar. 2016, pp. 1–8.
- [62] J. A. Tropp and A. C. Gilbert, "Signal recovery from random measurements via orthogonal matching pursuit," *IEEE Trans. Inf. Theory*, vol. 53, no. 12, pp. 4655–4666, Jan. 2008.
- [63] K. Guo, J. Jia, X. Yu, and L. Guo, "Dual-disturbance observers-based control of UAV subject to internal and external disturbances," in *Proc. CAC*, 2019, pp. 2683–2688.



Hang Ren (Graduate Student Member, IEEE) received the B.S. degree in electronic engineering from the University of Electronic Science and Technology of China (UESTC), Chengdu, China, in 2019, where he is currently pursuing the Ph.D. degree.

His research interests include synthetic aperture radar and evolutionary algorithms.



Zhichao Sun (Member, IEEE) received the B.S. and Ph.D. degrees in electronic engineering from the University of Electronic Science and Technology of China, Chengdu, China, in 2012 and 2017, respectively.

From 2016 to 2017, he was a Visiting Student with the Department of Electrical and Computer Engineering, Oklahoma State University, Stillwater, OK, USA. He was with Huawei Technologies Company Ltd., Shenzhen, China, from 2018 to 2019. He is currently with the University of Electronic Science and Technology of China. His research interests include synthetic aperture radar and evolutionary computation applications.



Jianyu Yang (Member, IEEE) received the B.S. degree in electronic engineering from the National University of Defense Technology, Changsha, China, in 1984, and the M.S. and Ph.D. degrees in electronic engineering from the University of Electronic Science and Technology of China (UESTC), Chengdu, China, in 1987 and 1991, respectively.

He is currently a Professor with the School of Information and Communication Engineering, UESTC. His research interests are mainly in synthetic aperture radar (SAR) and statistical signal processing.



Yuping Xiao (Student Member, IEEE) received the B.S. degree in electronic and information engineering from the University of Electronic Science and Technology of China (UESTC), Chengdu, China, in 2021, where she is currently pursuing the M.S. degree in information and communication engineering.

Her research interests include synthetic aperture radar (SAR) image processing.



Hongyang An (Graduate Student Member, IEEE) received the B.S. and Ph.D. degrees in electronic engineering from the University of Electronic Science and Technology of China, Chengdu, China, in 2015 and 2020, respectively.

From 2019 to 2020, he was a Visiting Student with Nanyang Technological University, Singapore. He is currently with the University of Electronic Science and Technology of China. His research interests include synthetic aperture radar and sparse signal processing.



Zhongyu Li (Member, IEEE) received the B.S. and Ph.D. degrees in electronic engineering from the University of Electronic Science and Technology of China (UESTC), Chengdu, China, in 2011 and 2017, respectively.

From 2015 to 2016, he was a Visiting Ph.D. Student with the Department of Information Engineering, Electronics and Telecommunications, Sapienza University of Rome, Rome, Italy. He is currently an Associate Professor with UESTC. His research interests include synthetic aperture radar technology (particular emphasis on synthetic aperture radar ground moving target detection and imaging).

Dr. Li is a Reviewer of the IEEE TRANSACTIONS ON GEOSCIENCE AND REMOTE SENSING, the IEEE GEOSCIENCE AND REMOTE SENSING LETTERS, and the *Journal of Electromagnetic Waves and Applications*.



Junjie Wu (Member, IEEE) received the B.S., M.S., and Ph.D. degrees in electronic engineering from the University of Electronic Science and Technology of China (UESTC), Chengdu, China, in 2004, 2007, and 2013, respectively.

From January 2012 to January 2013, he was a Visiting Student with the Department of Electrical and Computer Engineering, Duke University, Durham, NC, USA. He is currently a Professor with UESTC. His research interests include synthetic aperture radar imaging (particular emphasis on bistatic synthetic aperture radar).

Dr. Wu is also a Reviewer of IEEE TRANSACTIONS ON GEOSCIENCE AND REMOTE SENSING (TGRS), IEEE TRANSACTIONS ON SIGNAL PROCESSING (TSP), IEEE JOURNAL OF SELECTED TOPICS IN APPLIED EARTH OBSERVATIONS AND REMOTE SENSING (JSTARS), IEEE JOURNAL OF SELECTED TOPICS IN SIGNAL PROCESSING (JSTSP), IEEE GEOSCIENCE AND REMOTE SENSING LETTERS (GRSL), IET Radar, Sonar and Navigation (RSN), and so on.